

Sheet 25

HERCULE Test Bench - Confined Two-phase Gas-Solid Flow

SUMMARY

Sheet 25: HERCULE Test Bench - Confined Two-phase Gas-Solid Flow	547
25.1 TEST CASE DESCRIPTION	549
25.1.1 PURPOSE	549
25.1.2 SETUP DESCRIPTION	549
25.1.3 TEST DATA	551
25.1.4 REFERENCES	551
25.2 NUMERICAL SETUP	552
25.2.1 NUMERICAL MODELLING	552
25.2.2 MESH	552
25.2.3 BOUNDARY AND INITIAL CONDITIONS	554
25.2.4 NUMERICAL SCHEMES	558
25.2.5 USER CODING	558
25.2.6 CALCULATION STRATEGY	558
25.3 RESULTS	560
25.3.1 COMPUTING TIME AND PERFORMANCE	560
25.3.2 RUN DATA	560
25.3.3 COMPARISONS BETWEEN EXPERIMENTAL AND COMPUTED VALUES	568
25.4 ARCHIVING	577

EDF DIVISION R & D SERVICE MTI DÉPARTEMENT MFTT	Validation Report <i>Code_Saturne</i> Version 6.0.0	HI-83/01/006/P1 Page 548/750
---	---	---------------------------------

This page is intentionally blank

EDF DIVISION R & D SERVICE MTI DÉPARTEMENT MFTT	Validation Report <i>Code_Saturne</i> Version 6.0.0	HI-83/01/006/P1 Page 549/750
---	---	---------------------------------

HERCULE Test Bench - Confined Two-phase Gas-Solid Flow

Author : N. Picard - A. Douce (2004), RENUDA

Updated : 11/06/2020

Version & patches : Code_Saturne Version 6.0.2

Key-words : Lagrangian Two-Phase, Turbulent ($R_{ij} - \varepsilon$), two-way coupling, 2D axisymmetric.

25.1 Test Case Description

25.1.1 Purpose

The test case relates to two-phase flow of air with co-flowing particles in a configuration which is similar to those found in burners. A recirculation zone is created, which implies that gas-particles interaction happens both in the case where they both flow in the same direction and where they flow in opposite directions. The dispersed phase is poly-disperse. The particle loading is such that particles modify the air flow.

25.1.2 Setup Description

The geometry is presented in figure 25.1 and the flow is visualised in figure 25.2.

At the primary inlet, air and particles (glass spheres) are injected in the centre of the vertical, cylindrical pipe of length $1,5\text{ m}$ and radius $R_2 = 0,15\text{ m}$. Air is also injected in the annular, secondary inlet. The primary inlet has a radius of $R_j = 0,01\text{ m}$.

Several experimental cases are available ([3] and [9]). Amongst those, the case with a mass fraction of 22% ¹ has been selected for the simulations. Experimental data is available along the centre line and at different horizontal plane sections: $z = 0,003\text{ m}$, $z = 0,08\text{ m}$, $z = 0,16\text{ m}$, $z = 0,24\text{ m}$, $z = 0,32\text{ m}$, $z = 0,42\text{ m}$.

¹The thesis [9] also mentions cases with 11% and 110% mass loadings

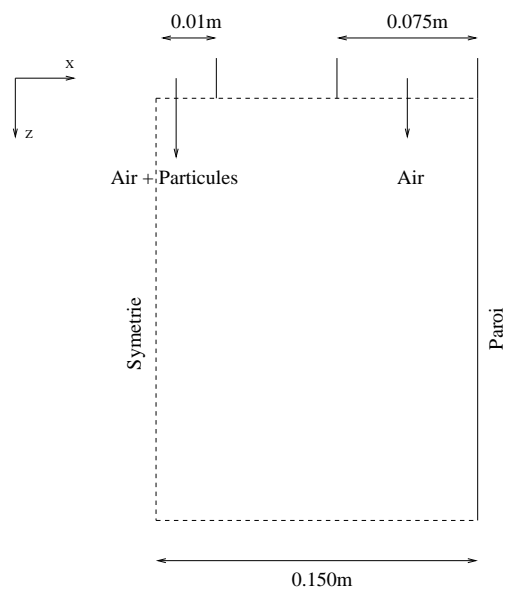


Figure 25.1: Test case geometry.

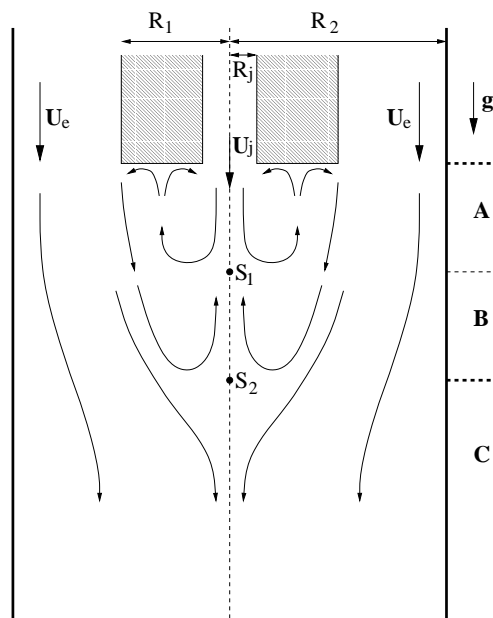


Figure 25.2: HERCULE experiment flow schematic.

25.1.3 Test Data

- Geometry and operating conditions:

Pipe diameter	0,3 m
Pipe length	1,50 m
Jet diameter	0,02 m
Jet maximum speed	4 m/s
Peripheral injection speed	6 m/s
Jet Reynolds number	3000

- Fluid properties

- dynamic viscosity: $\mu = 1,83337.10^{-5} \text{ kg.m}^{-1}.\text{s}^{-1}$
- density: $\rho = 1,17861 \text{ kg/m}^3$

- Particles properties (glass spheres):

Mean diameter d_p^μ	60 μm
Standard deviation σ_p	14,55 μm
Density ρ_p	2470 kg/m^3
Mass loading ϕ	0,22

The diameter of the particles, d_p , is computed based on the mean diameter and the standard deviation ² using the formula, $d_p = d_p^\mu + \xi\sigma_p$, where ξ is a random, non-imaginary variable following a normal law.

25.1.4 References

- [1] J.P. Minier, M. Ouraou, 'Module diphasique Lagrangien du code ESTET : calculs de validation et applications industrielles', *Rapport EDF*, HI-81/01/027/A 2001.
- [2] M. Ouraou, J.P. Minier, 'Modélisation Lagrangienne des écoulements diphasiques : prise en compte de l'influence des particules sur le fluide dans le module d'ESTET', *Rapport EDF*, HE-44/95/031/A 1995.
- [3] C. Vit, 'Modélisation eulérienne d'écoulements turbulents diphasiques gaz-solides présentant une granulométrie étendue de la phase dispersée.' *Rapport EDF*, HE-44/99/017/A 1999.

²The calculated diameter is kept bounded between 20 μm and 110 μm in order to avoid unphysical values which can occur from random sampling close to the edges of the Gaussian distribution (user program uslain.F).

- [4] J.P. Minier, E. Peirano, 'The PDF approach to turbulent polydispersed two-phase flows' *Physics Reports*, Vol. 352/1-3, pp. 1-214, September 2001 (Rapport EDF HI-81/01/025/A, 2001).
- [5] J. Pozorski, J-P. Minier, 'On the lagrangian turbulent dispersion models based on the langevin equation.' *Int. J. Multiphase Flow*, 24:913–945, 1998.
- [6] J. Pozorski, J-P. Minier, 'Probability density function modelling of dispersed two-phase turbulent flows.' *Physical Review E*, 59(1):855–863, 1998.
- [7] J-P. Minier, 'Closure proposals for the langevin equation model in Lagrangian two-phase flow modelling.' *Proceedings of the 3rd ASME/JSME Conference*, pages FEDSM99–7885, San Francisco, July 28-23 1999. ASME FED.
- [8] J.P. Minier, J. Pozorski, 'Analysis of existing Lagrangian models and new proposition for particule dispersion in homogeneous stationary turbulence.' *Rapport EDF* HE-44/92.29, 1992.
- [9] N. Caraman, 'Expérimentation modèle en écoulement gaz-solide co-courant confiné. Application de la modélisation eulérienne à l'analyse de l'influence du chargement en situation monodispersée ou polydispersée.' *Rapport EDF* HI-81/01/09/A, 2004.
- [10] A. Douce, J.P. Minier, 'Modélisation stochastique lagrangienne d'écoulements turbulents diphasiques dans *Code_Saturne*' *Rapport EDF* HI-81/04/03, 2004.

25.2 Numerical setup

25.2.1 Numerical modelling

- **Type of calculation :**

- Continuous phase: incompressible, turbulent, 2D axisymmetric, isothermal.
- Dispersed phase: solid particles, two-way coupling. Two different formulations are tested for the turbulent dispersion of the particles: The so-called “standard” and “complete” models.

- **Gravity:** Activated

- **Turbulence model:** $R_{ij} - \varepsilon$

25.2.2 Mesh

The mesh represents a 5° wedge. It is made of a single layer containing 8664 mesh cells. The origin is situated on the axis of revolution, in the inlet plane. The whole mesh and details of the mesh are shown in figure 25.3.

Type : Unstructured, hexahedral mesh with prismatic cells along the centre line.

Coordinate system: Cartesian³.

Number of cells : 8 664

Mesh construction methodology: SIMAIL mesher.

Calculation of the cells' centre of gravity: **NOTE TO PANOS: WE CAN PROBABLY GET RID OF THIS IN V6.** Normally, *Code_Saturne* would calculate the position of the cells' centre of gravity (cell centres we should probably say) using the cell faces' barycentres. However, for this case, it is necessary to calculate them using the position of the cell vertices to avoid problems with the calculations. This is done by adding the following code to the run script:

```
ECS_GRD_CDG_CEL_SOM=1
export ECS_GRD_CDG_CEL_SOM
```

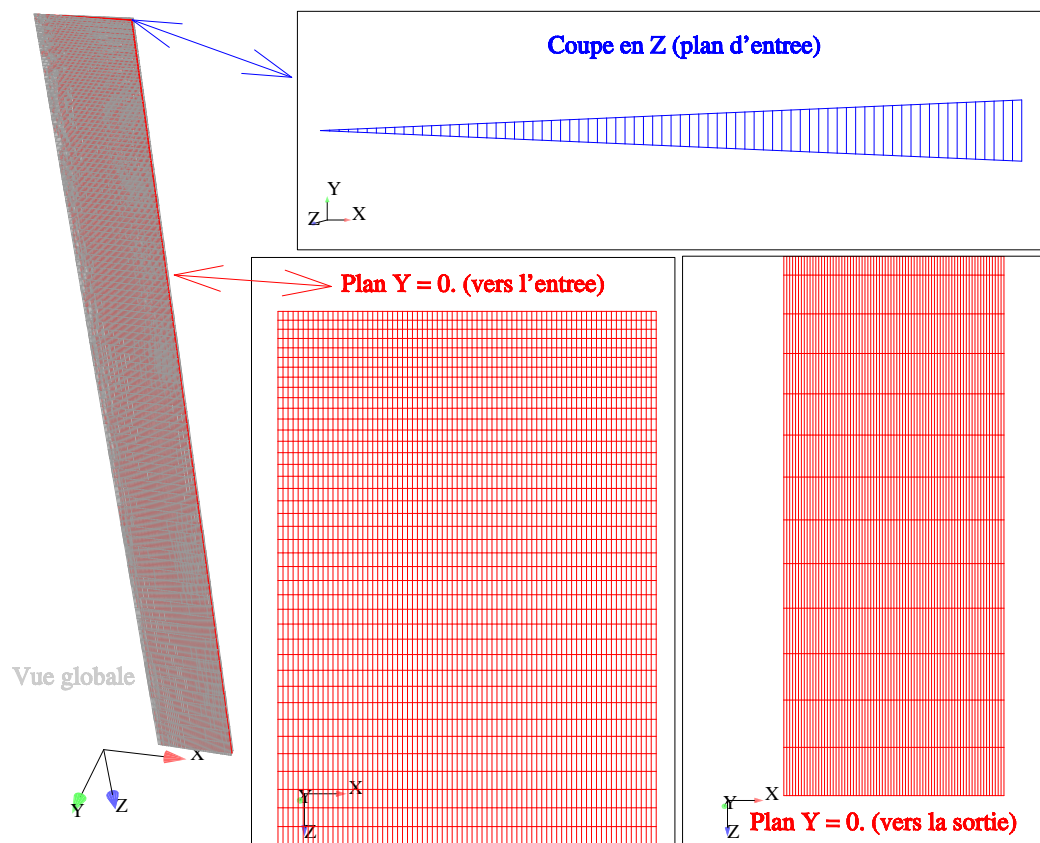


Figure 25.3: Mesh

³In the experiments, the measurements are done in a cylindrical system of coordinates. Therefore the data points must be converted to the mesh coordinate system (user codes inlet.F, inlet1.F and inlet2.F).

25.2.3 Boundary and Initial Conditions

- Specification of the boundaries and the boundary conditions for the fluid:

The different colours and the type of fluid boundary conditions given to the boundary faces are shown in figure 25.4.

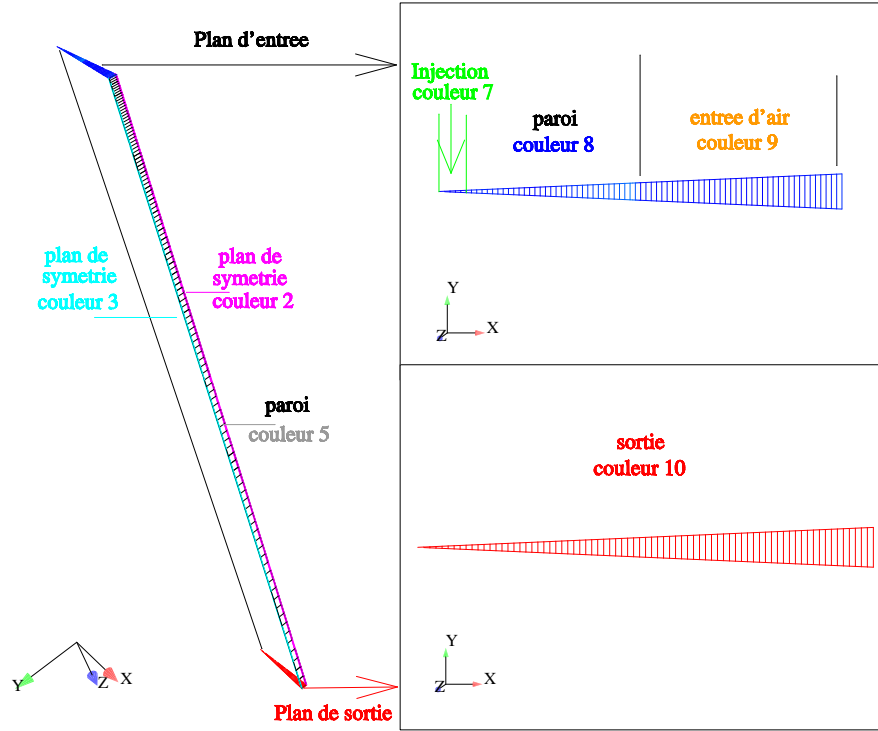


Figure 25.4: Boundary colours

- **Particles inlet data:**

The injection data of the particle cloud taken from the experimental data are listed in table 1. One may note that the fluctuations in radial and tangential velocity are identical.

The instantaneous velocity of the particles is calculated based on the mean velocity components and the velocity fluctuations $\mathbf{u}_p = (u_p, v_p, w_p)$. For each particle, an injection point is picked randomly in the injection plane. Depending on the injection point radius, the mean and fluctuation velocity components of the particle are first computed in the cylindrical coordinates system. The instantaneous velocity is then calculated based on drawing three random variables, η_1 , η_2 et η_3 following a normal distribution. The instantaneous particle velocity may then be calculated in the cylindrical coordinate system.

$$\begin{cases} u_{pr} = \langle u_{pr} \rangle + \eta_1 u'_{pr} \\ u_{p\theta} = \eta_2 u'_{p\theta} \\ u_{pz} = \langle u_{pz} \rangle + \eta_3 u'_{pz} \end{cases} \quad (u_{p\theta} = 0) \quad (1)$$

Coordinate radial <i>mm</i>	Velocity axial mean <i>m/s</i>	Velocity radial mean <i>m/s</i>	Velocity tangential mean <i>m/s</i>	Fluctuation velocity axial <i>m/s</i>	Fluctuation velocity radial <i>m/s</i>	Fluctuation velocity tangential <i>m/s</i>
0	3,989888	0,021573	0	0,492889	0,145902	0,145902
2	3,955918	0,019587	0	0,248873	0,153009	0,153009
4	3,818365	0,019053	0	0,276544	0,161393	0,161393
6	3,615492	0,018448	0	0,339334	0,174045	0,174045
8	3,235091	0,015862	0	0,45922	0,232101	0,232101
10	2,148246	0,098097	0	0,60341	0,198226	0,198226

Table 1: Dispersed phase distribution profiles.

The velocity is then converted to the mesh's Cartesian coordinate system:

$$\begin{cases} u_p = \cos\theta u_{pr} - \sin\theta u_{p\theta} \\ v_p = \sin\theta u_{pr} + \cos\theta u_{p\theta} \end{cases} \quad (2)$$

Similarly, the instantaneous fluid velocity is obtained from the experimental data in table 2: interpolation of the fluid velocity mean and fluctuating components at the cell centre, reconstruction of the instantaneous velocity, and conversion to the mesh's Cartesian coordinate system ⁴.

The particle injection mass flow rate is 1 *kg/h*. For the reduced, axisymmetric domain, this translates to 0,385.10⁻⁵ *kg/s*. This is equivalent to injecting 13.8 particles per time step in the computational domain, for 60 μm diameter particles and a 0,001 *s* time step. However, given the distribution of particle diameters, we chose to inject only 10 particles per time step. The statistical weight of each particle is then adjusted with regard to the mass flow rate.

- **Particle boundary conditions :**

region 1	colour 7	inlet
region 2	colours 10 et 9	outlet
region 3	colours 2, 3, 5 and 8	perfect rebound

- **Fluid velocity boundary conditions $\mathbf{u} = (u, v, w)$**

- **Inlet** : Dirichlet condition on the mean velocity components, the distribution profiles from the experiments are listed in table 2. The second component of

⁴By default, during the injection phase *Code_Saturne* uses the continuous phase's mean velocity as the fluid velocity which is seen by the particles. For this work, we have used the instantaneous fluid velocity.

the mean velocity, $\langle v \rangle$, is nought. ⁵. One may note that the fluctuations in radial and tangential velocity are identical.

Coordinate radial <i>mm</i>	Velocity axial mean <i>m/s</i>	Velocity radial mean <i>m/s</i>	Velocity tangential mean <i>m/s</i>	Fluctuation velocity axial <i>m/s</i>	Fluctuation velocity radial <i>m/s</i>	Fluctuation velocity tangential <i>m/s</i>
0	3,989888	0,043071	0	0,2206	0,165755	0,165755
2	3,955918	0,056412	0	0,235237	0,167099	0,167099
4	3,818365	0,071609	0	0,280546	0,188935	0,188935
6	3,615492	0,056304	0	0,345076	0,196318	0,196318
8	3,235091	0,067233	0	0,480505	0,199175	0,199175
10	1,15302	0,057133	0	0,462576	0,192527	0,192527
76	4,609382	-0,078698	0	0,620767	0,297634	0,297634
80	5,050922	-0,062107	0	0,412637	0,26486	0,26486
84	5,349239	-0,043911	0	0,378357	0,253143	0,253143
88	5,663382	-0,060412	0	0,33724	0,227446	0,227446
92	5,774033	-0,039152	0	0,309257	0,198263	0,198263
96	5,852311	-0,041603	0	0,268617	0,180068	0,180068
100	5,957135	-0,047923	0	0,26992	0,16104	0,16104
104	6,0781	-0,034075	0	0,248661	0,157479	0,157479
108	6,075214	-0,043817	0	0,239869	0,145587	0,145587
112	5,910082	-0,028827	0	0,24758	0,16021	0,16021
116	5,932579	-0,029241	0	0,238192	0,15885	0,15885
120	5,929479	-0,015086	0	0,31793	0,186978	0,186978
124	5,824071	0,017707	0	0,337416	0,201831	0,201831
127	5,773876	0,045791	0	0,338541	0,214657	0,214657

Table 2: Continuous phase profiles.

- **Free outlet:** zero flux, homogeneous Neumann condition.
- **Wall:** friction condition (two velocity scale wall model).
- **Symmetry:** symmetry.
- **Initial conditions :** $\langle u \rangle = 0$; $\langle v \rangle = 0$; $\langle w \rangle = 0$.
- **Pressure boundary conditions :**
 - **Inlet:** Homogeneous Neumann.
 - **Free outlet:** Standard condition.
 - **Wall:** Homogeneous Neumann.
 - **Symmetry:** Homogeneous Neumann.

⁵Although the experimental data is listed in a cylindrical reference frame, it is trivial to convert it in the Cartesian frame of the mesh since the two reference frames are aligned on the latter's axes.

EDF DIVISION R & D SERVICE MTI DÉPARTEMENT MFTT	Validation Report Code_Saturne Version 6.0.0	HI-83/01/006/P1 Page 557/750
---	---	---------------------------------

• **"Reynolds tensor" and "Turbulent dissipation" boundary conditions :**

- **Inlet:** Dirichlet condition. Given that only the velocity fluctuations are known, it is not possible to recalculate the cross-components of the Reynolds tensor. However, initialising only the diagonal to non-zero values using the measured fluctuating values whilst leaving the cross-components null leads to wrong results. Instead, it is necessary to use the turbulent kinetic energy to initialise the diagonal components and leave the cross-components at zero.

→ Kinetic turbulent energy from the experimental data:

$$k_{ent} = \frac{1}{2} \left(\langle u'^2 \rangle + \langle v'^2 \rangle + \langle w'^2 \rangle \right)$$

→ Reynolds tensor diagonal components:

$$R_{ii} = \frac{2}{3} k_{ent}$$

→ Reynolds tensor cross-components:

$$R_{ij} = 0$$

→ Turbulent dissipation based on the method programmed in **usclim.F** :

+ Primary inlet hydraulic diameter: $D_h = 0,02 \text{ m}$

+ Secondary inlet hydraulic diameter: $D_h = 0,15 \text{ m}$

+ The Reynolds number $Re = \frac{D_h V}{\nu}$ makes it possible to calculate the friction velocity, u^* , using the following formula:

$$u^* = V \sqrt{\frac{\lambda}{8}} \quad \text{avec} \quad \begin{cases} \lambda = 0,3164 Re^{-0,25} & \text{si } Re \leq 30000 \\ \lambda = 0,184 Re^{-0,2} & \text{si } Re \geq 30000 \end{cases}$$

+ Inlet turbulent dissipation:

$$\varepsilon_{ent} = C_\mu \frac{k_{ent}^2}{\kappa u^* 0,1 D_h}$$

where $C_\mu = 0,09$ and $\kappa = 0,41$ (constant of Kármán).

- **Free outlet:** Homogeneous Neumann.
- **Wall:** Turbulent wall model.
- **Symmetry plane:** Homogeneous Neumann. At the symmetry plane, it is necessary to activate the option to partially enable the calculation of the Reynolds tensor components: `ICLSYR(IPHAS) = 1`, for both the single and the two-phase flow calculations, otherwise the calculations converge towards unsatisfactory results. **NOTE RENUA, HOPEFULLY THIS IS NO LONGER NECESSARY SINCE THE SYM AND WEDGES ARE NOW WORKING WELL IN CS**
- **Initial conditions :** Automatically set based on $U_{ref} = 1 \text{ m/s}$.

25.2.4 Numerical schemes

25.2.5 User coding

- **usini1.F** : definition of the continuous phase physical parameters and the run parameters.
- **usclim.F** : definition of the continuous phase boundary conditions as a function of the border faces colours (figure 25.4).
- **uslag1.F** : definition of the dispersed phase physical parameters and the Lagrangian run parameters.
- **uslag2.F** : definition of the dispersed phase boundary conditions as a function of the border faces colours (figure 25.4).
- **uslain.F** : definition of the injection profiles of the particles.
- **uslast.F** : Creation and formatting of the output files compatible with *xmgr* to plot the particles profiles.
- **usproj.F** : Creation and formatting of the output files compatible with *xmgr* to plot the fluid profiles.
- **inlet.F, inlet1.F et inlet2.F** : programs to interpolate the experimental data at the inlet.
- **lagopt.F** : Non-user program, kept here to correct a test on the two-way coupling.
- **reseps.F** : Non-user program, kept here to remove the explicit component of the dispersed phase two-way coupling effect on the continuous phase turbulent dispersion to ensure robustness ⁶.

25.2.6 Calculation strategy

The runs are carried out in two steps. The first step is a single phase calculation, without particles. This makes it possible to initialise the two-phase calculation and, later, to quantify the influence of the particles on the flow.

Two, two-phase calculations have been run, one for each turbulent dispersion model, namely the so-called "standard" and "complete" models.

• Single phase calculation

- **Restart:** NO
- **Total number of time steps:** 2000
- **Time step:** constant (IDTVAR=0), 10^{-3} s

⁶This is necessary, otherwise the calculations do not run.

• **Two-phase calculations**

- **Restart:** YES
- **Restart of the Lagrangian calculation:** NO
- **Total number of additional time steps:** 5000 (i.e. the number of Lagrangian steps)
- **Time step:** (IDTVAR=0), 10^{-3} s
- **Stationary continuous phase:** YES (ISTTIO=1)
- **Turbulent dispersion model:**
 - * For the first two-phase calculation: "standard" model, starting from the first Lagrangian step (MODCPL=0)
 - * For the second two-phase calculation : "complete" model, starting from the first Lagrangian step (MODCPL=1 and IDIRLA=3)
- **Dynamic two-way coupling:** YES (IILAGR=2 and LTSDYN=1)
- **Time averaging of the two-way coupling terms:** YES, starting from Lagrangian step 1500 (NSTITS=1500); figure 25.9 shows that the particle loading in the calculation domain may be considered as complete by that step
- **Calculation of volumetric statistics:** YES (ISTALA=1) from the first Lagrangian step (IDSTNT=1)⁷
- **Time averaging of the volumetric statistics:** YES, starting at Lagrangian 2000 (NSTIST=2000); figure 25.9 indicates that this is reasonable.
- **Total number of particles injected at each time step:** 10

Remarks RENUDA : Contrary to the calculation of CS 1.1.1, the two-phase calculation with the "standard" model here runs with the first order for the integration for the stochastic differential equations (with CS 1.1.1 it was the second order). The second order crashes with CS 6.0.2 after few iterations. And for the "complete" model, the first order for the integration for the stochastic differential equations was used for the same reason than for the "standard" model and it was necessary to uncheck the particle turbulent dispersion option.

	DIPH-STD $R_{ij} - LRR$	DIPH-CPL $R_{ij} - LRR$
Order for the integration for the stochastic differential equations	first order	first order
Particle turbulent dispersion option	ticked	unticked

Table 3: Options used with CS 6.0.2

⁷It is necessary to activate the calculation of the volumetric statistics in order to use the "complete" model.

25.3 Results

25.3.1 Computing time and performance

Machine : Two machines have been used:

the machine clcathy at Clamart : VPP5000

a x86 platform - OS : Linux - frequency = 2,6 GHz

Compilers : frt (VPP5000) ; g77 (x86)

Total CPU time :

- Single phase calculation : 1204 s (VPP5000)
- Two-phase "standard" calculation : 23297 s (x86)
- Two-phase "complete" calculation : 24171 s (x86)

Time per cell and per time step :

- Single phase calculation : $6,910^{-5}$ s (VPP5000)
- Two-phase "standard" calculation : $5,4.10^{-4}$ s (x86)
- Two-phase "complete" calculation : $5,6.10^{-4}$ s (x86)

Memory :

- precision: DOUBLE
- memory used by integers (IA):
 - Single phase calculation : 341 781 entiers
 - Two-phase "standard" calculation : 605 863 entiers
 - Two-phase "complete" calculation : 605 863 entiers
- memory used by real numbers (RA):
 - Single phase calculation : 2 114 397 réels
 - Two-phase "standard" calculation : 3 804 186 réels
 - Two-phase "complete" calculation : 3 882 162 réels

25.3.2 Run data

- Single phase run
 - Inlet flow at the outlet: NO
 - No "reversal of conditions" at the wall
 - Number of clips on $R_{ij} - \varepsilon$: none
 - Number of wall faces in laminar flow: 0
 - Number of wall faces in turbulent flow: 147
 - Maximum CFL number of the order of 1.75 (very stable)

- Minimum CFL number of the order of $0,5 \cdot 10^{-2}$ (slight oscillation)

- **"standard" two-phase run**

- Inlet flow at the outlet: NO
- No "reversal of conditions" at the wall
- Number of clips on $R_{ij} - \varepsilon$: none
- Number of wall faces in laminar flow: 0
- Number of wall faces in turbulent flow: 147
- Maximum CFL number of the order of 1.75 (very stable)
- Minimum CFL number of the order of $0,4 \cdot 10^{-2}$
- Percentage of lost particles: 0,05%

- **"complete" two-phase run**

- Inlet flow at the outlet: NO
- No "reversal of conditions" at the wall
- Number of clips on $R_{ij} - \varepsilon$: none
- Number of wall faces in laminar flow: 0
- Number of wall faces in turbulent flow: 147
- Maximum CFL number of the order of 1.75 (very stable)
- Minimum CFL number of the order of $0,4 \cdot 10^{-2}$
- Percentage of lost particles: 0,07%

- **Single phase run convergence**

Figure 25.6 shows the time history of the axial and radial components of the mean velocity, the diagonal terms of the Reynolds tensor, and the turbulent dissipation recorded at 15 different points (table 4 and figure 25.5)

Globally, the graphs show that the calculations are converged within the 2000 iterations. Although, probes F and G display oscillations around a mean value. This can be explained by the probes' position just upstream of the separation of the two inlets in the recirculation zone. As the oscillations are stable, the run is considered converged.

- **Two-phase runs convergence**

For the two, two-phase runs, figures 25.7 and 25.8 show the time histories of the continuous phase mean velocity axial and radial components, the Reynolds stresses R_{11} , R_{22} , R_{33} and the dissipation. For clarity of the figures, the oscillations at probes F and G are not shown on all the graphs.

The graphs indicate that the two-phase runs may be considered converged by time step 3500^{ième}.

<i>A</i>	$x = 0,02 \quad z = 0,89.10^{-2}$
<i>B</i>	$x = 0,02 \quad z = 0,49.10^{-1}$
<i>C</i>	$x = 0,02 \quad z = 0,25$
<i>D</i>	$x = 0,02 \quad z = 0,5$
<i>E</i>	$x = 0,02 \quad z = 1$
<i>F</i>	$x = 0,07 \quad z = 0,89.10^{-2}$
<i>G</i>	$x = 0,07 \quad z = 0,49.10^{-2}$
<i>H</i>	$x = 0,07 \quad z = 0,25$
<i>I</i>	$x = 0,07 \quad z = 0,5$
<i>J</i>	$x = 0,07 \quad z = 1$
<i>K</i>	$x = 0,12 \quad z = 0,89.10^{-2}$
<i>L</i>	$x = 0,12 \quad z = 0,49.10^{-1}$
<i>M</i>	$x = 0,12 \quad z = 0,25$
<i>N</i>	$x = 0,12 \quad z = 0,5$
<i>P</i>	$x = 0,12 \quad z = 1$

Table 4: Probe coordinates (m)

- **Total number of particles in the computational domain**

Figure 25.9 shows the time history of the total number of particles in the computational domain for both two-phase runs. The number of particles stabilises by the 1500^{ième} Lagrangian step.

The maximum number of particles obtained in the two runs is different, of the order of 7200 particles in the "standard" run compared to about 6600 for the "complete" run between steps 1500 et 2200, and 5600 after step 3000. The difference observe may be due to the fact that the particle velocity fluctuations predicted but the "complete" model of turbulent dispersion are larger than for the "standard" model (figures 25.16 and 25.17).

For the "complete" run, the change in the total number of particles between steps 2200 and 3000 is likely related to the fact that the time averaging of the particle volumetric statistics (which plays a role in the "complete" model formulation) starts at Lagrangian step 2000. The full effect of the kicking-off of the time averaging takes place over a relaxation duration of about 200 steps.

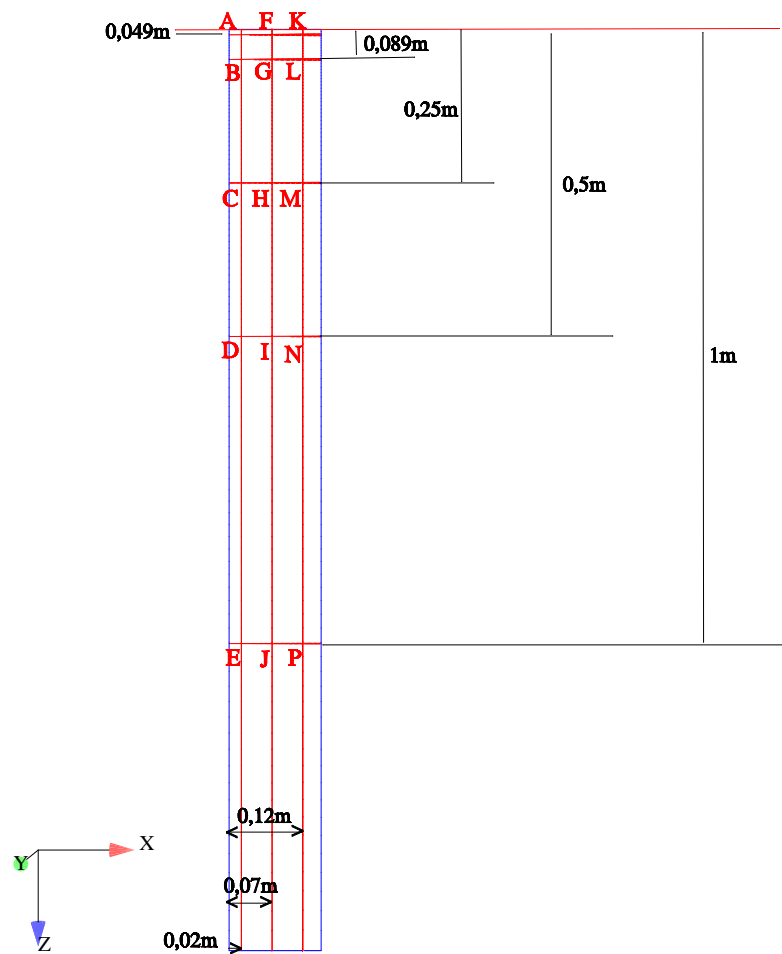


Figure 25.5: Probe locations.

MONO Rij-LRR

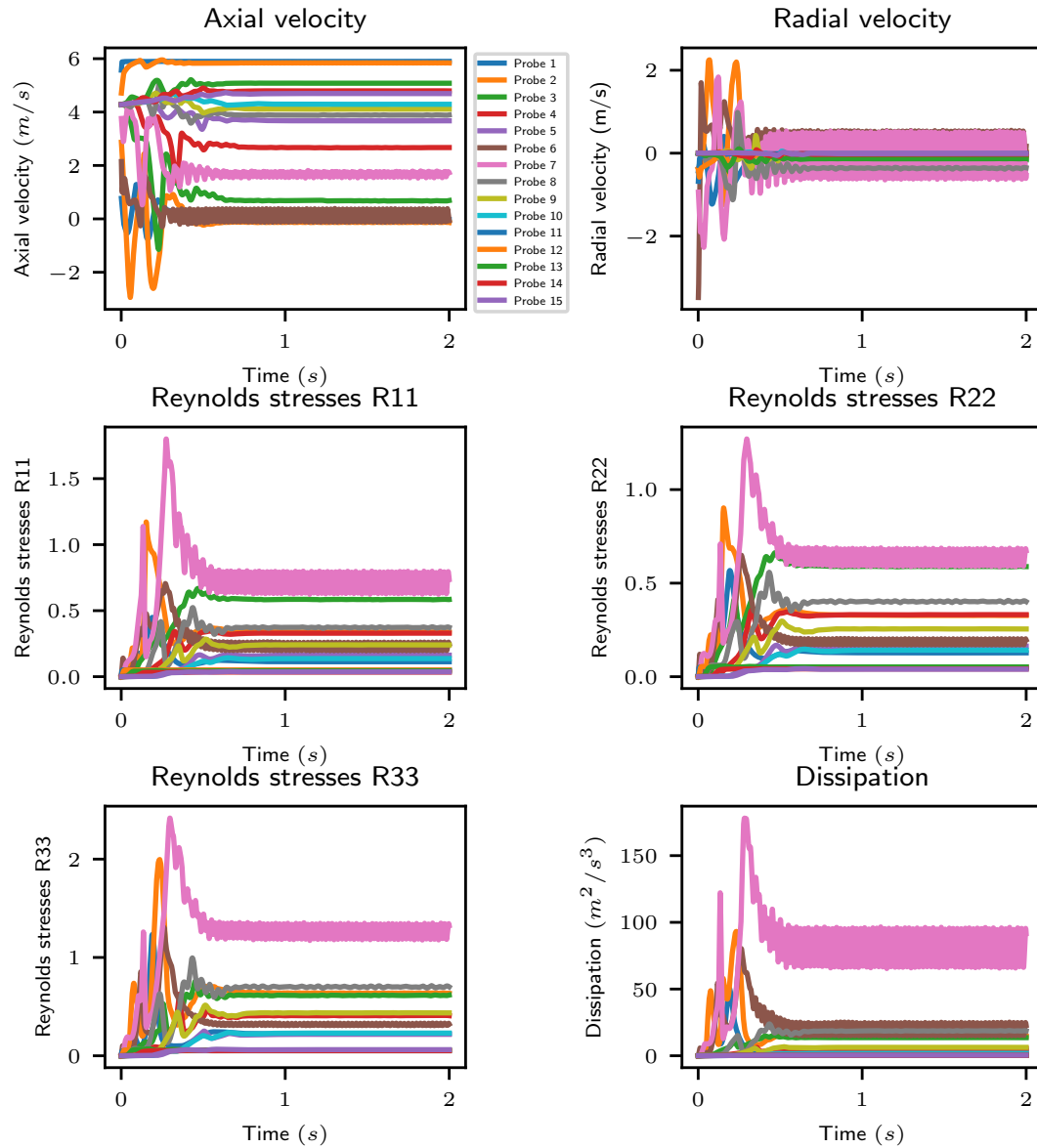


Figure 25.6: Single phase calculation: convergence history of the axial and radial mean velocity components, Reynolds stresses R_{11} , R_{22} , R_{33} and the dissipation.

DIPH-STD Rij-LRR

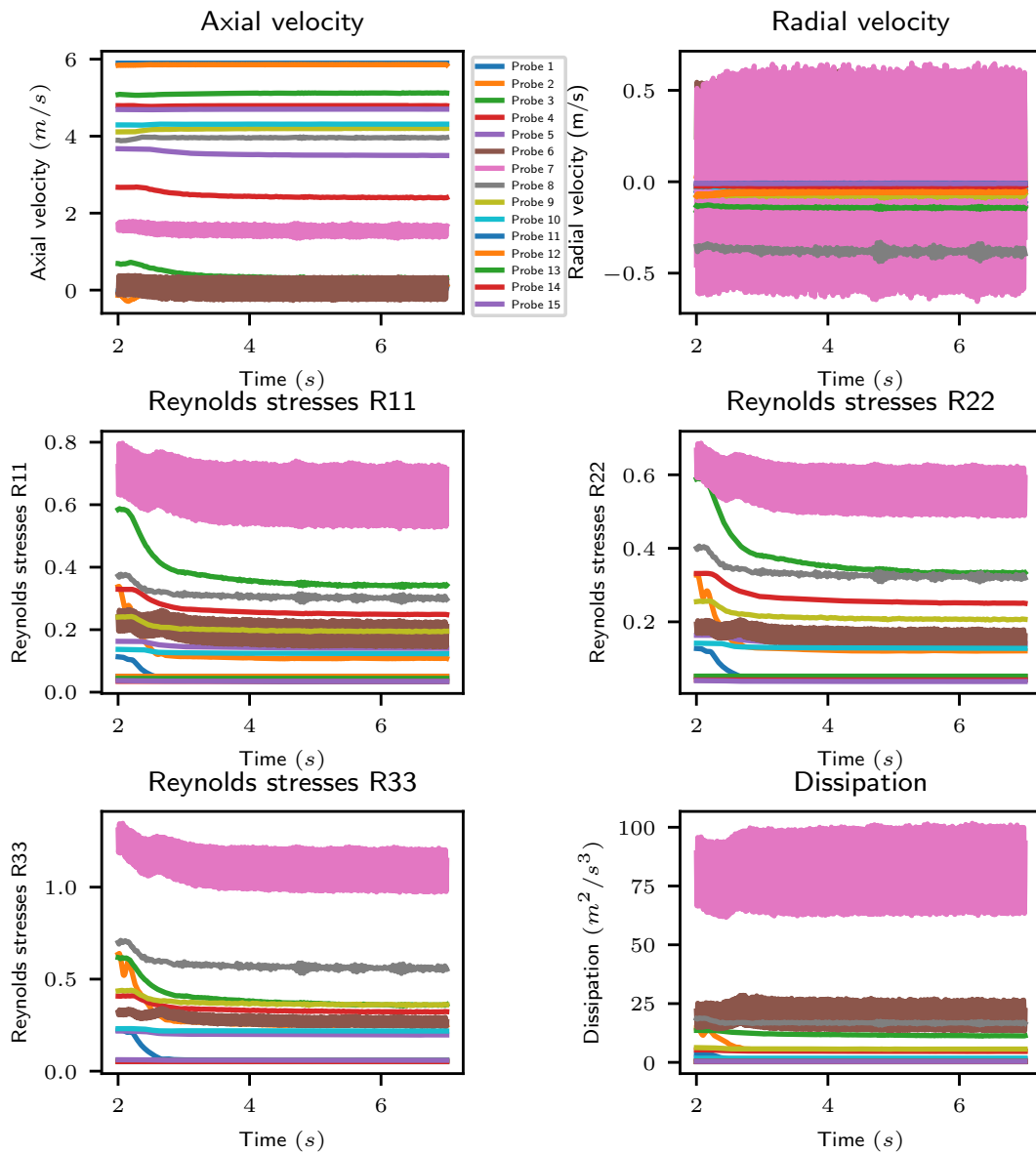


Figure 25.7: "standard" two-phase run: convergence history of the mean velocity axial and radial components, the Reynolds stresses R_{11} , R_{22} , R_{33} and the dissipation.

DIPH-CPL Rij-LRR

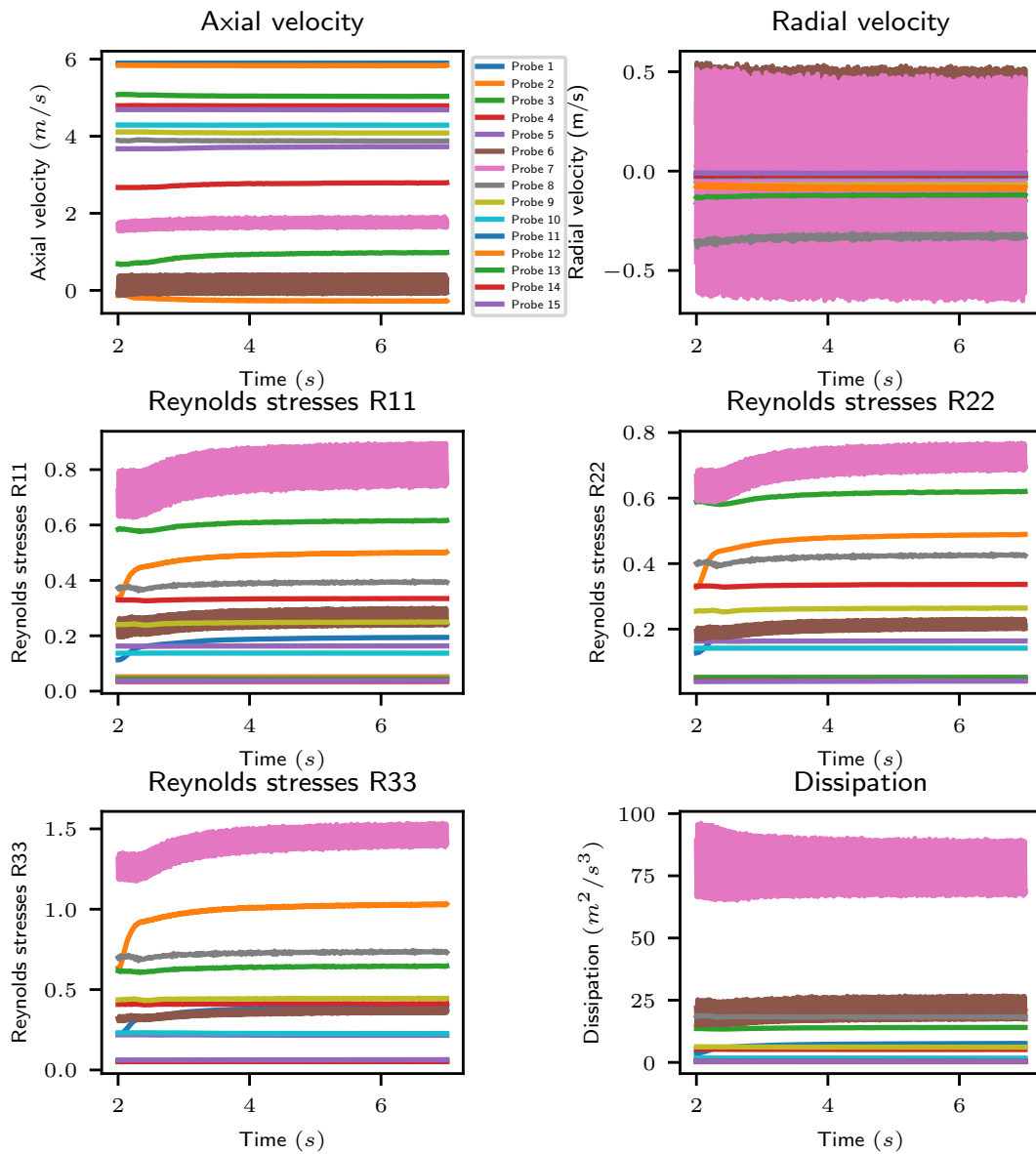


Figure 25.8: "complete" two-phase run: convergence history of the mean velocity axial and radial components, the Reynolds stresses R_{11} , R_{22} , R_{33} and the dissipation.

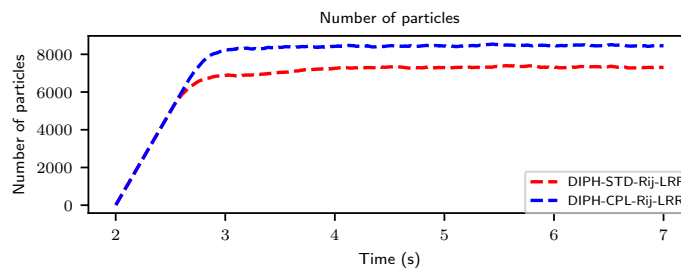


Figure 25.9: Time evolution of the total number of particles in the computational domain.

25.3.3 Comparisons between experimental and computed values

25.3.3.1 Single-phase run

The measured and computed mean velocity axial components are compared along the z axis in figure 25.10 and along horizontal plane sections at $z = 0,003\text{ m}$, $0,08\text{ m}$, $0,16\text{ m}$, $0,24\text{ m}$, $0,32\text{ m}$, $0,42\text{ m}$ in 25.11.

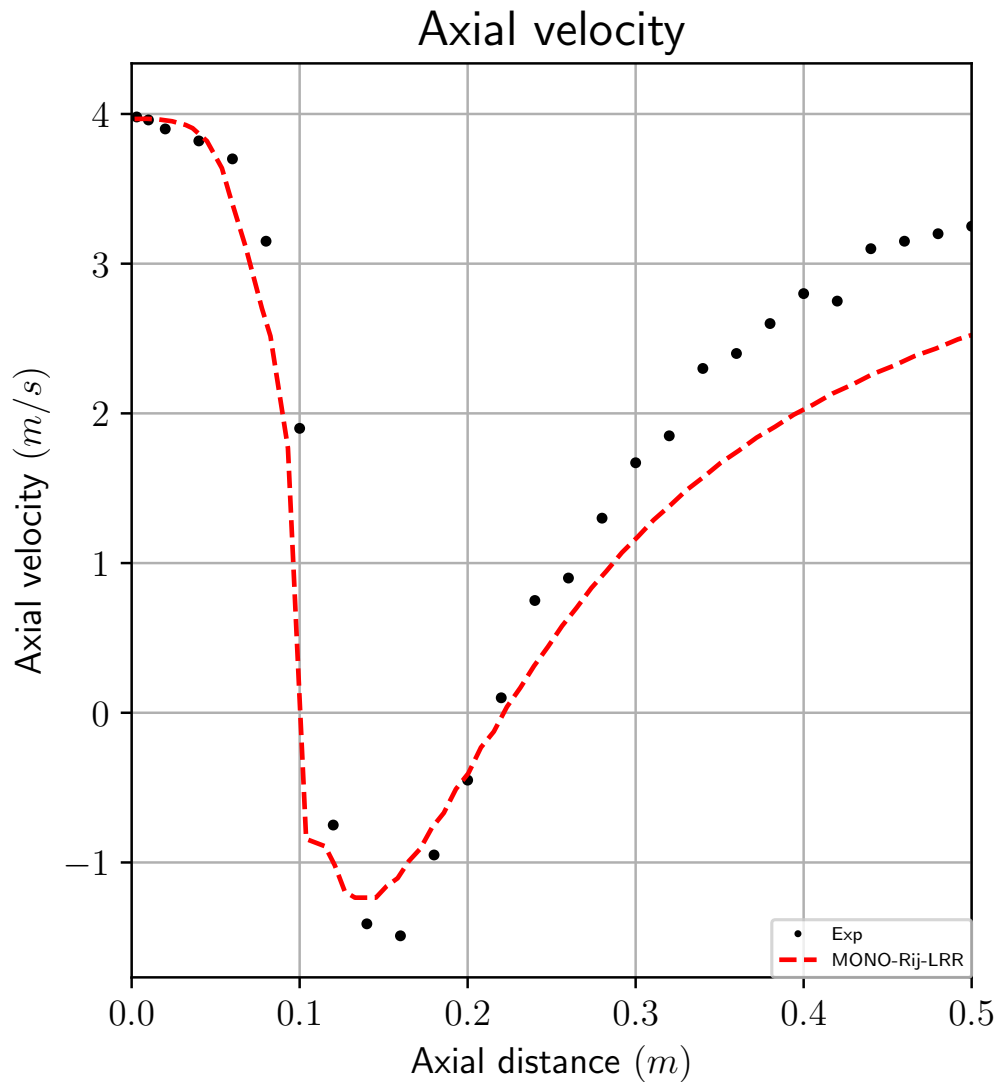


Figure 25.10: Single phase run: fluid mean velocity axial component along the centre line.

Looking at the graph, the flow is divided in three large regions which are separated by the two stagnation points denoted $S1$ and $S2$ on figure 25.10. The first region, (called A on figure 25.2) situated between the primary inlet and the first stagnation point is representative of the central jet penetration. The calculation gives a reasonable prediction. The second region (called B on figure 25.2), located between the two stagnation points represents the recirculation zone. The calculation gives a good prediction, particularly with regard to the position of points $S1$ and $S2$. The minimum velocity is slightly

underestimated. The third zone (called C on figure 25.2) denotes the zone where the annular flow reaches the axis of symmetry and evolves towards a free jet flow. The results from the run are offset from the experimental results in this zone. Whilst the offset is also evident on the radial profiles at $z = 0,32\text{ m}$ and $z = 0,42\text{ m}$ in figure 25.11, it is smaller. In any case, according to [3], there are reasons to question the experimental measurements in this region.

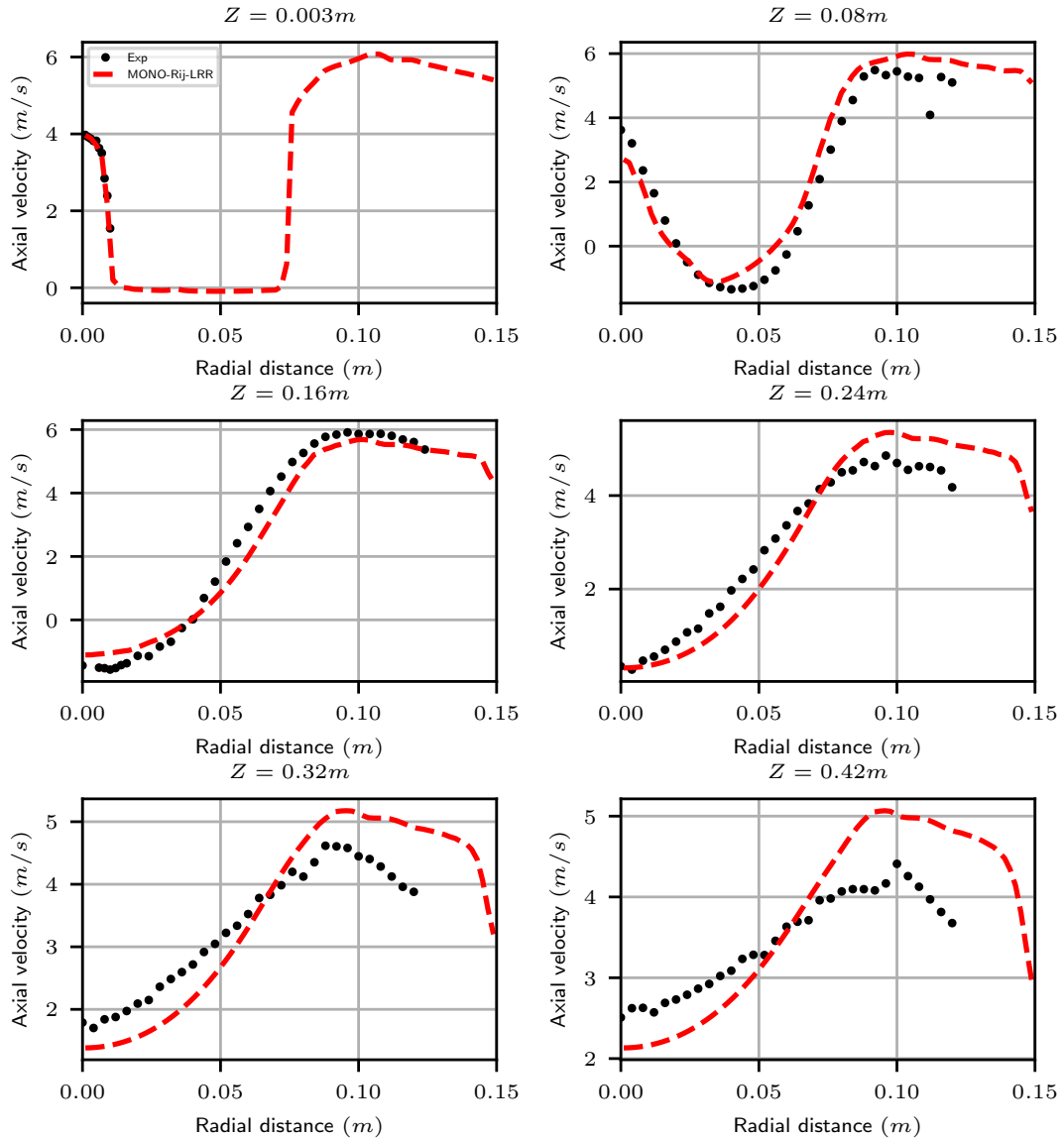


Figure 25.11: Single-phase run: fluid mean velocity axial component profiles at the different measurement plane sections.

25.3.3.2 Two-phase runs

- **Continuous phase :**

Figures 25.12 and 25.13 show the calculated continuous phase mean velocity axial component. Figure 25.12 shows the profiles along the centre line, z , whereas figure 25.13 shows the profiles along the plane sections at $z = 0,003\text{ m}$, $0,08\text{ m}$, $0,16\text{ m}$, $0,24\text{ m}$, $0,32\text{ m}$, $0,42\text{ m}$.

Globally, the continuous phase flow predictions do not differ much between the single phase run and the "standard" and "complete" two-phase runs. Figure 25.12) indicates that the two runs do not give correct predictions of the first two zones: the penetration length of the primary inlet jet is underestimated whereas it is the opposite for the length of the recirculation zone between the two stagnation points. The comparisons in the transversal plane sections show that the difference between the measured and computed values is significant mostly in a zone very close to the centre line. Figure 25.13 shows as well that the quality of the predicted values deteriorates with distance from the inlets.

- **Dispersed phase :**

The calculated mean dispersed phase velocity axial and radial components are shown in figures 25.14 and 25.15 along the plane sections at $z = 0,003\text{ m}$, $0,08\text{ m}$, $0,16\text{ m}$, $0,24\text{ m}$, $0,32\text{ m}$, and $0,42\text{ m}$. Figures 25.16 et 25.17 show the fluctuation dispersed phase velocity axial and radial components.

Away from the external edges of the particle cloud (near the edges of the measuring points), the calculated mean axial velocities are in acceptable agreement with the experimental ones. However, the results for the mean radial velocity are more questionable, although they have a reasonable order of magnitude. The peaks observed in the curves near a radial distance of 0.1 m and above come from a few isolated particles on the edge of the particle clouds. Therefore, in these zones, the means are computed on the basis of few samples and should be considered with caution.

With regard to the axial component of the fluctuating particle velocity, the "complete" run shows superior predictions compared to the "standard" one. Globally, it yields satisfactory predictions. The situation is less clear for the radial component of the velocity fluctuation, particularly along the plane sections at $z = 0,24\text{ m}$ and $0,32\text{ m}$. However, here too, the "complete" run gives better results than the "standard" one.

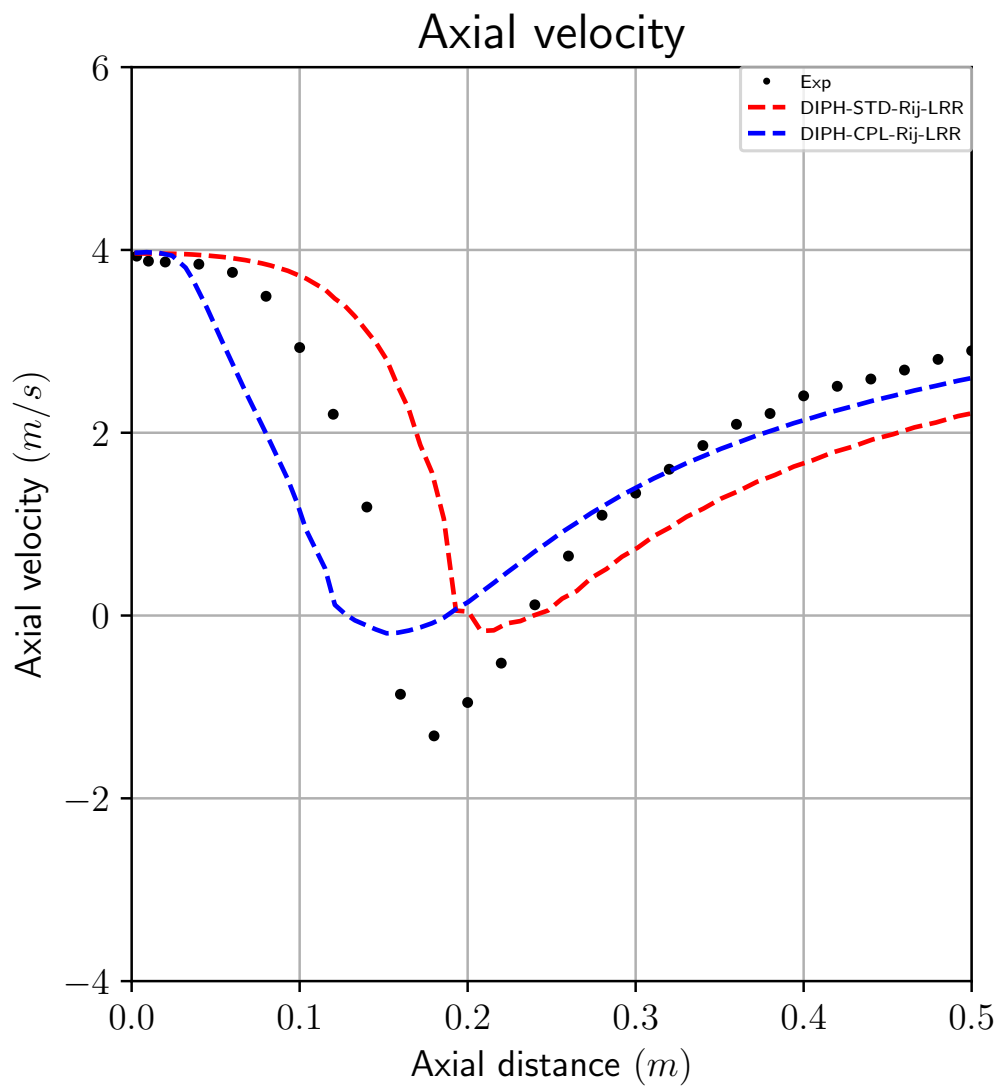


Figure 25.12: Two-phase run: mean fluid velocity axial component along the centre line.

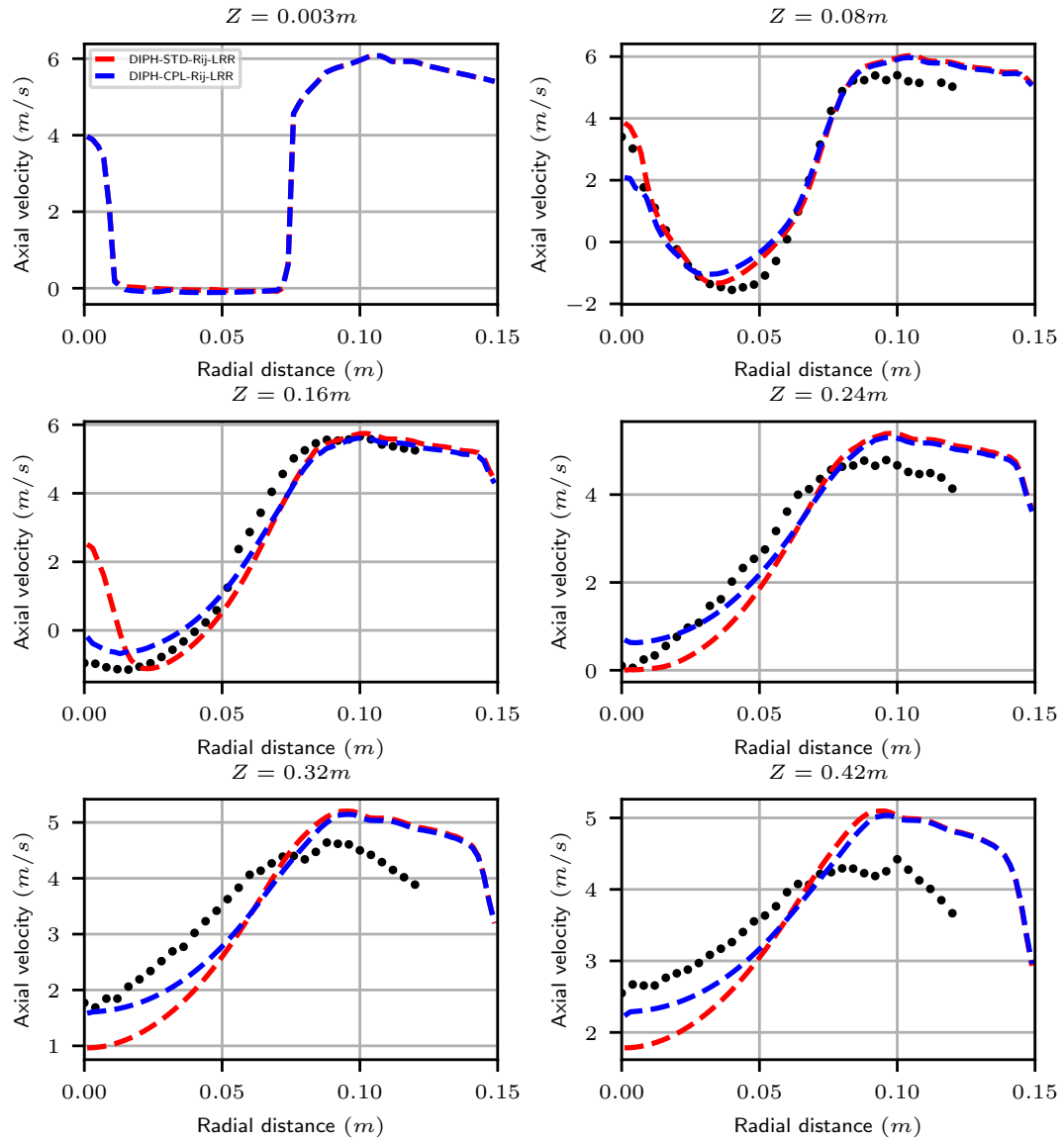


Figure 25.13: Two-phase run: mean fluid velocity axial component profiles along the different measurement planes.

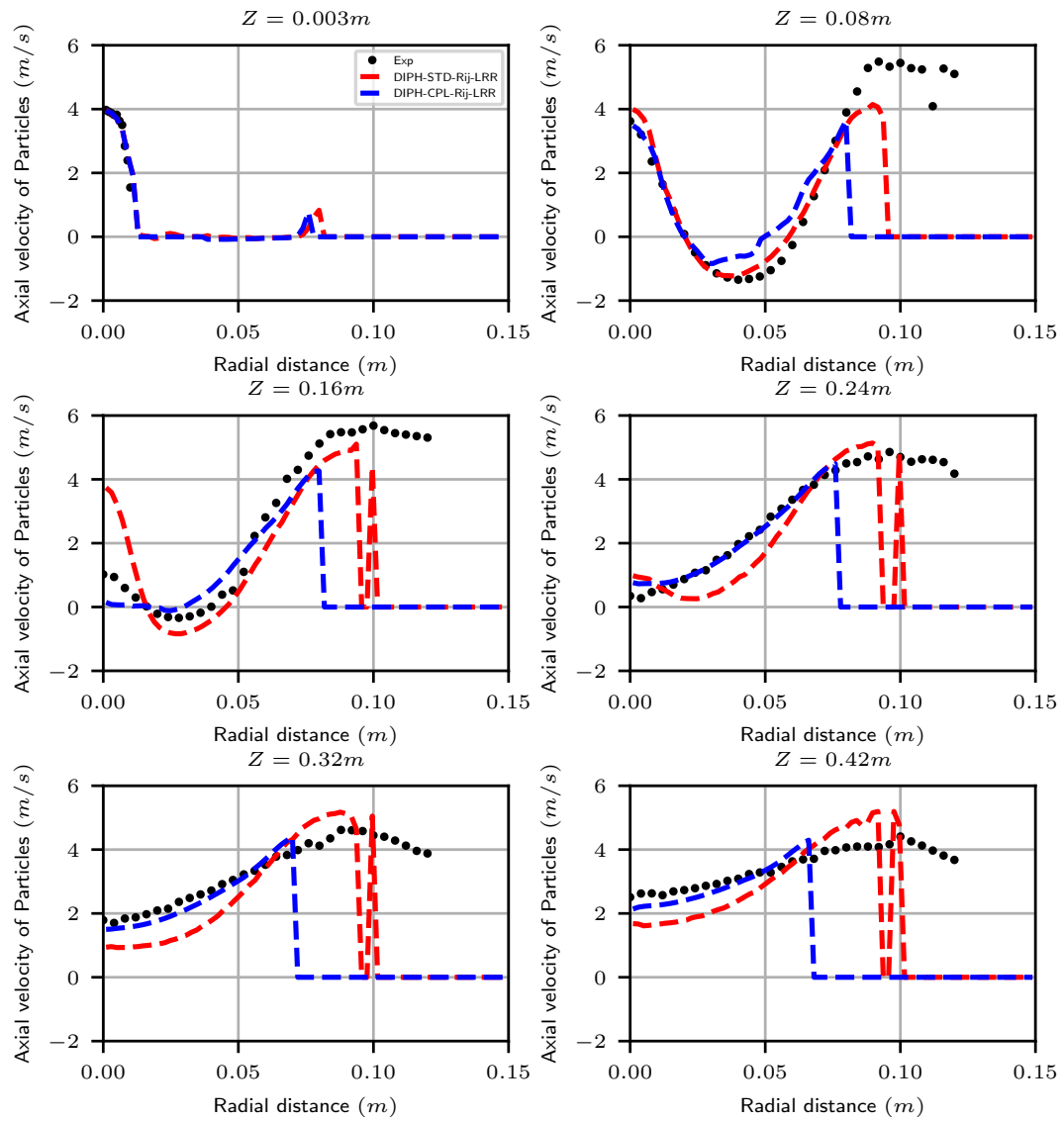


Figure 25.14: Two-phase run: profiles of the mean particle velocity axial component along the different measurement plane sections.

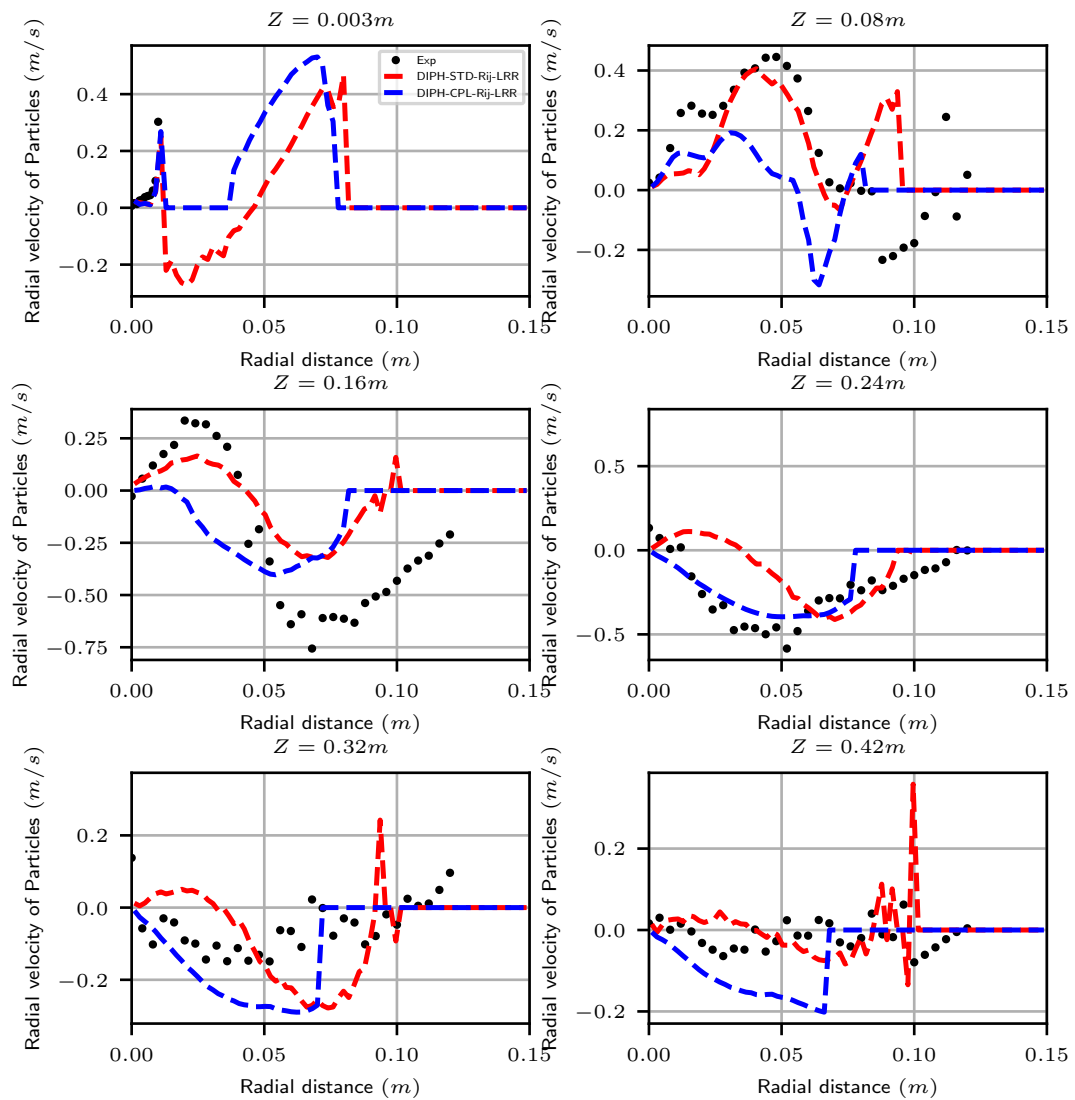


Figure 25.15: Two-phase run: profiles of the mean particle velocity radial component along the different measurement plane sections.

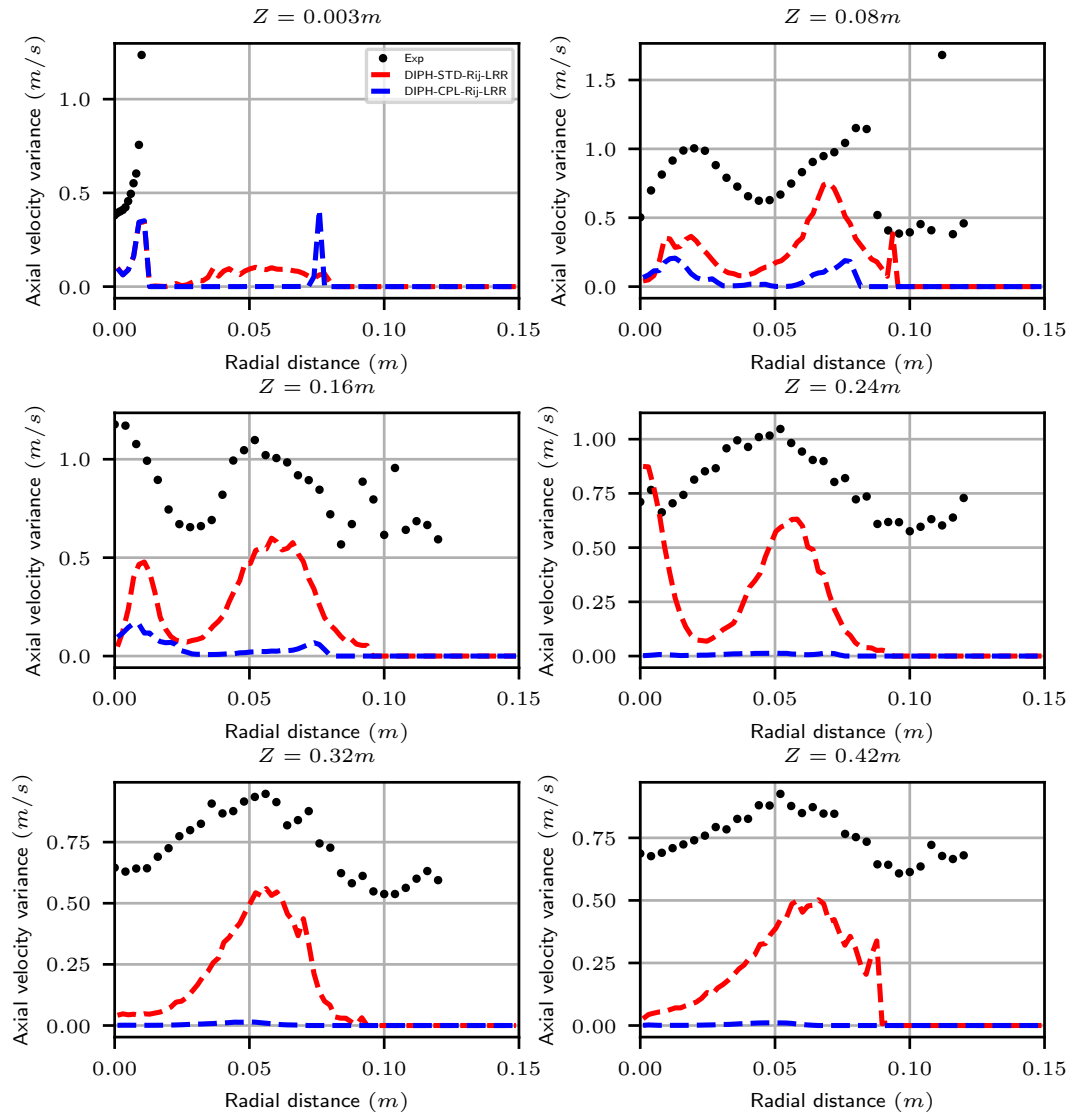


Figure 25.16: Two-phase run: profiles of the fluctuating particle velocity axial component along the different measurement plane sections.

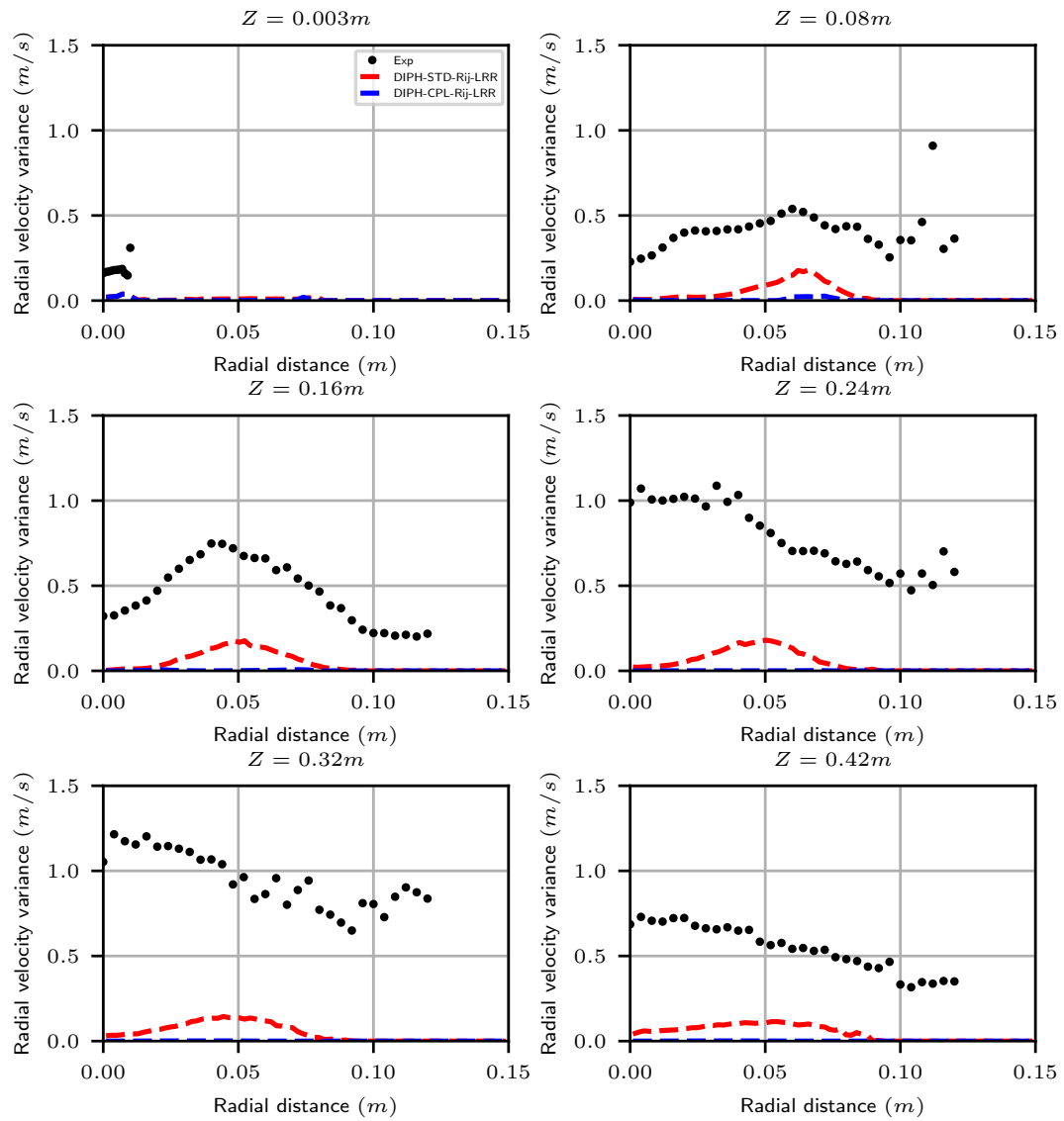


Figure 25.17: Two-phase run: profiles of the fluctuating particle velocity radial component along the different measurement plane sections.

EDF DIVISION R & D SERVICE MTI DÉPARTEMENT MFTT	Validation Report <i>Code_Saturne</i> Version 6.0.0	HI-83/01/006/P1 Page 577/750
---	---	---------------------------------

25.4 Archiving

The directory for the case is named: **HERCULE**

The sub-directories are organised as follows:

MONO: everything having to do with the single-phase calculation.

DIPH_STD: everything having to do with the "standard" two-phase calculation.

DIPH_COMPLET: everything having to do with the "complete" two-phase calculation.

POST: all the profiles which have been plotted using *xmgr*.

EDF DIVISION R & D SERVICE MTI DÉPARTEMENT MFTT	Validation Report <i>Code_Saturne</i> Version 6.0.0	HI-83/01/006/P1 Page 578/750
---	---	---------------------------------

This page is intentionally blank